Halo uncertainties in electron recoil events at direct detection experiments

Tarak Nath Maity,[a,*] **Tirtha Sankar Ray,**[a,b,†] **Sambo Sarkar**[b,‡]

[a] *Department of Physics, Indian Institute of Technology Kharagpur, Kharagpur 721302, India*
[b] *Centre for Theoretical Studies, Indian Institute of Technology Kharagpur, Kharagpur 721302, India*

Abstract

The dark matter direct detection rates are highly correlated with the phase space distribution of dark matter particles in our galactic neighbourhood. In this paper we make a systematic study of the impact of astrophysical uncertainties on electron recoil events at the direct detection experiments with Xenon and semiconductor detectors. We find that within the Standard Halo Model there can be upto $\sim 35\%$ deviation from the fiducial choice in the exclusion bounds for these uncertainties. For non-standard halo models motivated by N-body simulations we report conservative modifications of standard exclusion bounds that are correlated with the dynamics of the underlying simulation.

1 Introduction

In the last few decades particulate dark matter (DM) has been probed by its possible scattering with the Standard Model (SM) particles [1–5]. The typical direct detection experiments measure the nuclear recoil of a target material through scattering of ambient DM wind on the surface of the earth [1,2,6–9]. While nuclear target experiments are suitable to probe a DM mass at $\mathcal{O}(100)$ GeV, however for DM masses in sub-GeV range these looses its sensitivity. This is due to the fact that energy deposited by a sub-GeV non-relativistic DM remains below the threshold of these experiments.

An alternate and novel strategy to search for such light DM is through the DM-electron scattering [10–14]. For an atomic target (e.g Xenon) if DM scatters off the electron on the atomic shell then this may lead to the ionization of electrons. Whereas for a semiconductor target material (e.g. Si, Ge etc.) scattering of DM with electron may transferred an electron from valance band to conduction band. These ionization signals could provide a handle in the search for sub-GeV DM. The boundedness of electron in the target material makes these electron scattering events inelastic in nature. This essentially suggests that the incoming DM particles has to have a sufficient energy to excite these bound electron. For a semiconductor material the typical energy gap between valance and conduction band is of the order 1 eV whereas for Xe targets the minimum binding energy of a shell is around 10 times larger than that. Thus for a Xe target materials a relatively light DM can excite an electron

*tarak.maity.physics@gmail.com
†tirthasankar.ray@gmail.com
‡sambosarkar92@gmail.com

if the DM is moving fast. These fast moving DM can only be found near the tail of the galactic DM distribution. Subsequently the DM-electron event rate would be suppressed for such Xe targets as compared to semiconductors targets, implying sensitivity of semiconductor detector below the MeV scale.

The DM-electron scattering rate can be divided into three parts viz. particle physics, atomic physics and astrophysics. The particle physics input depends on the particular model under consideration and determines the hard scattering cross section between the DM and the electron. In this paper we take a model independent approach to estimate the cross sections. The electron ionization form factor constitutes the atomic physics part and depends on the wave function of the scattered electron. For this we have used the result of QEdark [15]. In QEdark, the form factor for Xe targets has been calculated using Hartee-Fock method while for semiconductor materials density functional theory has been utilized.

The local distribution of the ambient DM constitutes the astrophysical part. The Standard Halo Model (SHM) with Maxwell-Boltzmann (MB) distribution truncated at galactic escape velocity is usually assumed for the distribution of DM in the galaxy. The dispersion of the MB distribution is determined by the Sun's circular velocity (v_0). The typical choice of these parameters are $v_0 = 220$ km/s and $v_{\rm esc} = 544$ km/s, following [16]. However there is still a considerable uncertainty in the measurement of these astrophysical inputs [17]. Recent cosmological N-body simulations suggest that the local distribution of the DM may deviate from the MB distribution. In this paper we make a systematic study of the impact of these astrophysical uncertainties in DM electron scattering rate.

N-body simulations indicate that the SHM may not give an accurate description of a Milky Way-like halo. There have been attempts to find empirical fitting functions to better capture the phase space within N-body and hydrodynamic simulations [18, 19] as well as parametrizations to match astrophysical observations and N-body simulations [20, 21]. These include the Double power law which can nicely explain the high velocity dependence of double power density profiles like that of NFW [22]. The Mao et. al. [23] suggests another distribution showing a strong correlation of particle velocities to their position and characteristic radius of the simulated halo [23]. The King velocity distribution determines the cut off in the distribution through a self consistent manner [24]. The Tsallis is a theoretical distribution based on Gibbs entropy motivated Tsallis statistics [25]. In this work we have only considered isotropic distributions while leaving the possible impact of anisotropic distributions [26] for a future work.

The paper is organized as follows. In section 2 we briefly review the methodology to calculate rate of the DM-electron scattering for atomic and semiconductor target material. In section 3 we present the variations of DM-electron exclusion limit due to the uncertainty in the SHM parameters. Going beyond, in section 4 we explore the effect of non-standard velocity distribution. Finally we conclude in 5.

2 DM-electron scattering

In this section we will briefly review the scattering of DM particles with electrons that are bound inside the detector material. We will pair it down to the particle physics effects, the atomic physics effects and the astrophysical factors. Let us consider a DM particle (χ) of mass m_χ, and initial velocity v scatters of an electron within the target material. Then in the non-relativistic limit the energy

conservation of the system implies

$$\Delta E_e + \frac{|m_\chi \mathbf{v} - \mathbf{q}|^2}{2m_\chi} = \frac{1}{2} m_\chi v^2, \tag{1}$$

where q is the momentum transfer by DM and ΔE_e is the energy transferred to electron. Note that for a DM mass in sub-GeV scale, the relevant momentum transfer is small compared to the mass of the nucleus, therefore the nuclear recoil piece has been neglected in equation (1)[1]. Following equation (1), the minimum DM speed $v_{\rm min}$ required to transfer a energy ΔE_e for a fixed q is given by

$$v_{\rm min} = \frac{q}{2m_\chi} + \frac{\Delta E_e}{q}, \tag{2}$$

For an atomic target (e.g. Xenon) the differential DM-electron scattering rate is

$$\frac{dR_{\rm ion}}{d\,ln\,E_e} = N_T \frac{\rho_\chi}{m_\chi} \sum_{nl} \frac{\overline{\sigma}_e}{8\mu_{\chi e}^2} \int q dq\, F_{\rm DM}(q)^2\, |f_{\rm ion}^{n,l}(k',q)|^2\, \eta\left(v_{\rm min}(k',q)\right), \tag{3}$$

where N_T denotes the number of atoms in the target. ρ_χ is the local DM density. DM-electron reduced mass is denoted by $\mu_{\chi e}$. $\overline{\sigma}_e$ stands for DM-electron cross section for a particular momentum transfer $q = \alpha m_e$ and $F_{\rm DM}$ is the DM form factor. The ionization form factor and average inverse velocity are represented by $f_{\rm ion}^{\rm n,l}$ and η respectively.

Whereas, the differential rate for a semiconductor target (e.g. Ge) can be written as

$$\frac{dR_{\rm crystal}}{d\,ln\,E_e} = \frac{\rho_\chi}{m_\chi} N_{\rm cell} \overline{\sigma}_e \alpha \frac{m_e^2}{\mu_{\chi e}^2} \int d{\rm ln}q\, \frac{E_e}{q}\, F_{\rm DM}(q)^2\, |f_{\rm crystal}(k',q)|^2\, \eta\left(v_{\rm min}(k',q)\right), \tag{4}$$

where $N_{\rm cell}$ stands for the number of unit cell in a crystal targets [12]. The $f_{\rm crystal}$ denotes the ionization form factor for the crystal.

Note that both in equations (3) and (4) $F_{\rm DM}(q)$ takes care of the momentum dependency in DM-electron interaction. This DM form factor and $\overline{\sigma}_e$ comprise the main particle physics input in equations (3) and (4). Remaining agnostic about any particular model here we have considered three types of interactions between DM and electron. These interactions can be quantified by the DM form factor $F_{\rm DM}$. The three choices for the $F_{\rm DM}$ are 1, $\alpha m_e/q, (\alpha m_e/q)^2$. Note that $F_{\rm DM} = 1$ can be induced by an exchange of heavy mediator between DM and electron [27, 28], $F_{\rm DM} = \alpha m_e/q$ which could arise through electric dipole moment interaction [29], and $F_{\rm DM} = (\alpha m_e/q)^2$ which may be induced by a light mediator [12, 27].

The ionization form factor defines the suppression of the event rate to ionize an electron from its bound state to a continuum state of momentum $k' = \sqrt{2 m_e E_e}$ through q. Hence it depends solely on the target material. Throughout our numerical calculation we have utilized the form factor given in QEdark [15].

Other than these the usual astrophysical inputs are the local DM density ρ_χ and average inverse DM speed

$$\eta(v_{\rm min}) = \int_{v_{\rm min}}^{\infty} \frac{f_\oplus(\mathbf{v})}{v} d^3 v, \tag{5}$$

[1]The typical momentum transfer to electron is of the order of few keV and the nuclear mass is of the order GeV. Therefore the recoil nuclear energy remains below eV.

The $f_\oplus(\mathbf{v})$ in equation (5) is the DM velocity distribution in the detector rest frame. If we assume $f(\mathbf{v})$ as the DM distribution in the galactic frame then the distribution at lab frame can be obtained by

$$f_\oplus(\mathbf{v}) = f(\mathbf{v} + \mathbf{v_e}), \tag{6}$$

where $\mathbf{v_e} = \mathbf{v_0} + \mathbf{v}_\circledast + \mathbf{v}_\oplus$ and $\mathbf{v_0}$ and $\mathbf{v}_\circledast$ are the Sun's circular velocity at local standard rest and Sun's peculiar velocity respectively. The earth velocity in the Solar rest frame is represented by $\mathbf{v}_\oplus$. Note that the variation in $\mathbf{v}_\oplus$ with time leads to the familiar annual modulation [12, 13] in the DM direct detection rate, has been neglected here. The sun's peculiar motion $\mathbf{v}_\circledast = (U_\circledast, V_\circledast, W_\circledast) = (11.1 \pm 1.5, 12.2 \pm 2, 7.3 \pm 1)$ is adapted from [30]. We set the earth's rotational velocity following reference [6].

The mean inverse speed is essentially regulated by the astrophysical parameters discussed above. Therefore any uncertainty in determination of these parameters will have a direct impact in the exclusion limit. Further, several high resolution cosmological N-Body simulations suggest that the DM velocity distribution may depart for standard MB distribution [22, 31, 32], particularly in the high velocity tail region [22]. In the rest of this paper we systematically study the impact of these astrophysical uncertainties including departure from the MB distribution on the exclusion bounds of direct detection experiments.

The differential rates given in equations (3) and (4) are with respect to the electron recoil energy E_e. While the semiconductor detectors are only sensitive to electron and the Xe detector finally detects photo-electron at the PMT's. For the Xe target material this electronic energy is converted into a number of electrons and subsequently to photo-electrons using the prescription of [14]. Note that the Xenon10 experiment [33] sets most stringent limits in most of the region of the parameter space interest [14], therefore we would only consider the bound from Xenon10 in this paper. Whereas for semiconductor targets the electron-hole yields are obtained following reference [12]. Since the one electron threshold sets the most stringent bound in the relevant parameter space [12], we assume the same to present the bound for semiconductor detectors.

3 Astrophysical uncertainties within the Standard Halo Model

The most simplified isotropic and isothermal DM distribution in the halo is usually described by a MB distribution, with a cut off at the escape velocity of the DM particles for the Milky Way like halo [34, 35]. The distribution function has the following form

$$f(\mathbf{v}) = \begin{cases} \frac{1}{N}\left[\exp\left(-\frac{|\mathbf{v}|^2}{v_0^2}\right)\right] & |\mathbf{v}| \leq v_{\rm esc} \\ 0 & |\mathbf{v}| > v_{\rm esc}, \end{cases} \tag{7}$$

where N denotes the Normalization constant of the distribution, v_0 is the measure of its velocity dispersion and $v_{\rm esc}$ sets the maximum allowed DM velocity of the distribution. Keeping ourselves within this SHM, in this section we will present the uncertainties in the determination of astrophysical parameters and their implications on the dark electron scattering events[2]. A discussion about the main observational uncertainties in the SHM parameters are now in order:

[2]Note that for semiconductor material the astrophysical uncertainties within SHM have been studied previously in reference [36, 37],

1. **Local DM density:** The typical choice for the local density is 0.3 GeV cm^{-3} [38]. Recent estimations suggest that it may vary in the range $(0.2-0.6)$ GeVcm^{-3} [17, 26, 39–41]. However note that the differential rate given in equations (3) and (4) scale linearly with the local DM density. Therefore for a change in ρ_χ one would expect a proportional vertical shift in the exclusion limits for all the experiments. Assuming the central value of the local DM density 0.4 GeV cm^{-3}, we find that there is a maximum 100% relative change due to the aforementioned variation of ρ_χ. This change is independent of the DM mass and the target materials used for the detection. Hence we have fixed this to 0.4 GeV cm^{-3} without considering its variational implications on the exclusion bounds.

2. **Circular velocity of the Sun:** The local circular velocity of the Sun (v_0) with respect to the galactic center is usually assumed to be 220 km/s [7, 42, 43]. This would be considered as the fiducial choice of the parameter v_0 for rest of the paper. From the orbit of the GD-1 stellar stream, the reference [44] constrained v_0 in the range 221 ± 18 km/s. A similar range of v_0, namely 225 ± 29 km/s is found to be in consonance with the kinematics of maser [45]. These estimates seem to have around 10% error in the measurement of v_0. However a more precise assessment of v_0 can be done using the measurement of apparent proper motion of Sgr A* relative to a distant quasar [46, 47]. This measurement fixes the total angular velocity of the Sun $((v_0+V_\circledast)/R_\odot)$ in the range 30.24 ± 0.12 km s^{-1}kpc^{-1}. On the other hand recently GRAVITY collaboration has estimated the value of $R_\odot$ with quite a high accuracy: 8.122 ± 0.031 kpc [48]. Also note that the relevant component of the peculiar velocity $V_\circledast$ varies in the range 12.24 ± 2.47 [30]. Combining all these observations, the circular velocity of the Sun has been found to be 233 ± 3 km/s [26]. We will explore the impact of the deviations of this from the fiducial value on the exclusion from direct detection experiments in the electron scattering events.

   As can be seen from the equation (7), v_0 is related to the standard deviation of the distribution. Thus any increment in v_0 would flatten the distribution. Therefore this would make more DM particles available to interact with electrons in the tail region. This will lead to a relatively stronger bound in DM-electron cross section. The effect will be reversed for a decrement in v_0. Further a change in v_0 would also alter the Galilean boost.

3. **Galactic escape velocity:** The escape velocity of a massive body in a galaxy is defined by the velocity above which they will no longer remain bound to its gravitational potential. Measurements from the high velocity stars of the RAVE survey determines the $v_{\rm esc}$ in the range $498-608$ km/s [16] with the median 544 km/s. In the rest of the paper we would consider this as the fiducial choice for $v_{\rm esc}$. Based on the recent analysis of the velocities of 2850 halo stars from the *Gaia* velocity survey Data Release-2 [49], the local escape speed has been revised to 580 ± 63 km/s. However it has been argued that this result is sensitive to the prior chosen for describing high velocity tail of the distribution function. With a prior estimation from simulations, and a more localized sample of 2300 high velocity counter-rotating stars, the escape speed has been obtained to be 528^{+24}_{-25} km/s [50]. This is also in consonance with the previous results. We will be using the central value of the latter as the new central value for the escape velocity of the DM particles within the SHM.

To estimate the relative fractional change in the cross-section we will adopt equation (8) throughout this paper,

$$\Delta = \left|\frac{\overline{\sigma}_e^{\rm i} - \overline{\sigma}_e^{\rm fiducial}}{\overline{\sigma}_e^{\rm fiducial}}\right|, \tag{8}$$

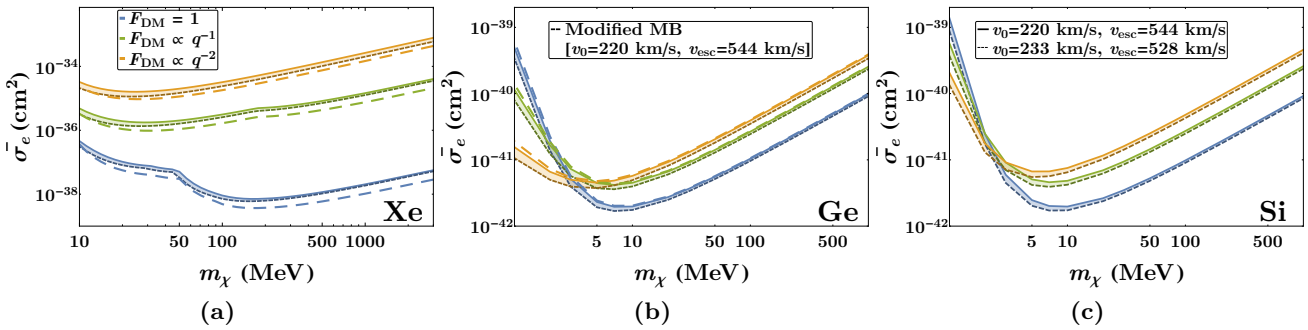

Figure 1: Variation in the SHM from recent astrophysical observations. For each panel the solid curves represent the exclusion bound for the fiducial values of $v_{\rm esc} = 544$ km/s and $v_0 = 220$ km/s . The dashed curves represent the bounds from the recent astrophysical observations with $v_{\rm esc} = 528$ km/s and $v_0 = 233$ km/s. The Blue, Green and Yellow shaded regions express the astrophysical uncertainties for $F_{\rm DM} = 1,\ \alpha m_e/q$ and $(\alpha m_e/q)^2$ respectively. The exclusion bounds for Modified MB distribution (given in equation (9)) with fiducial values are shown by extra spaced dashed lines. (a) The left panel is for an atomic Xe target material. The central (b) and right (c) panels show the variations for a Germanium and Silicon semiconductor target material respectively.

where $\overline{\sigma}_e^{\rm i}$ denotes the cross section corresponding to non-fiducial values of the distribution in consideration.

With a decrease in the escape velocity there will be less energetic particles in the halo capable of scattering, hence a larger σ_n is required to produce the same number of events at a given experiment. Note that due to exponential suppression of the MB distribution near the tail, increasing $v_{\rm esc}$ has a smaller effect than decreasing it by the same amount. We find that for similar relative change in v_0 and $v_{\rm esc}$, the effect due to the change in v_0 is more pronounced. This can be ascribed to the fact that any changes in v_0 causes an overall change in the shape of distribution, whereas the $v_{\rm esc}$ determines the distribution's cut-off near the exponentially suppressed tail.

The inverse relation between m_χ and $v_{\rm min}$ implies that the required minimum DM velocity is rather close to $v_{\rm esc}$ for light DM. This is because DM particles having lower mass and hence lower kinetic energy can generate certain recoil energy if their minimum velocity becomes closer to the escape velocity of the distribution. And the tail of the distribution is quite sensitive to the choice of astrophysical parameters. Thus the observed fractional change in the exclusion limit is significantly larger for light DM. This is evident from all figures shown in the paper.

In figure 1, the light solid lines represent the exclusion curves for the fiducial set of values and the dashed lines represent the exclusion bounds for the recent astrophysical observations of $v_{\rm esc} = 528$ km/s and $v_0 = 233$ km/s. The blue, green and yellow shaded regions figure 1 represents the deviations from the fiducial values for the three choices of the DM form factor $F_{\rm DM} = 1,\ \alpha m_e/q$ and $(\alpha m_e/q)^2$ respectively. Like figure 1, in rest of the paper the variations of a Xenon target are shown in the left panel, whereas similar variations for Germanium and Silicon target materials are depicted in the middle and right panels respectively. In conclusion our study indicates a maximum of $\Delta \sim 35\%$ deviation due to astrophysical uncertainties in the velocity distribution. This is over and above the modifications due to the ambiguity in the measurement of the local DM density mentioned earlier.

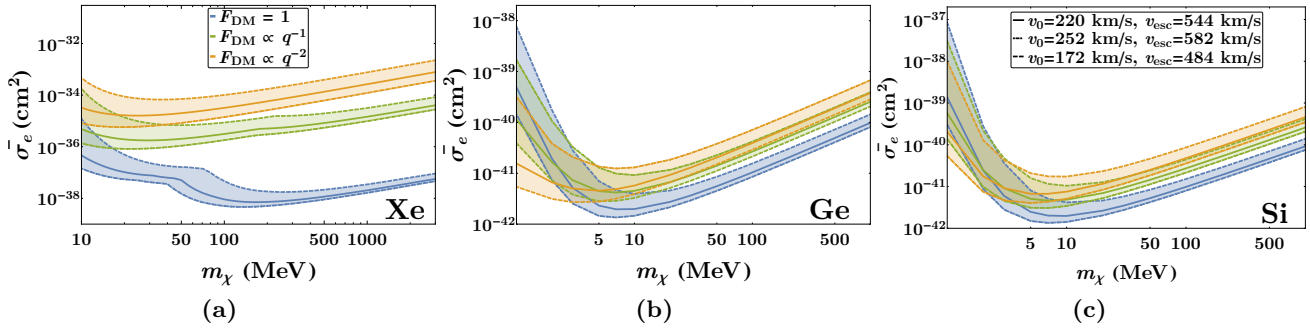

Figure 2: Variation in the SHM from the IllustrisTNG N-body simulation [36]. The dashed curves represent the exclusion bounds for $v_{\rm esc} = 484$ km/s and $v_0 = 172$ km/s and the dot-dashed curves represent the exclusion bounds for $v_{\rm esc} = 582$ km/s and $v_0 = 252$ km/s. The other relevant details are mentioned in figure 1.

3.1 N-body simulation

An alternate way to estimate the value of v_0 and $v_{\rm esc}$ is to fit a model of DM velocity distribution to cosmological N-body simulations. Here we have adapted the result of [36], which has utilized the data of the IllustrisTNG Cosmological simulation [51] to find the best-fit values. The quoted maximum and minimum values of the concerned parameters are $v_{\rm esc} = [584,\ 432]$ km/s, $v_0 = [252,\ 172]$ km/s respectively. We have employed these set of values to present the shift in the exclusion bounds as shown in figure 2. The blue, green and yellow shaded regions represent the uncertainties associated with the aforementioned variations in v_0 and v_{esc} for $F_{\rm DM} = 1$, $\alpha m_e/q$ and $(\alpha m_e/q)^2$ respectively. The solid lines represent the exclusion bounds for the fiducial choice of v_0 and $v_{\rm esc}$. We observe a maximum change $\Delta \sim \mathcal{O}(10)$ in the cross section relative to the SHM.

3.2 Modified Maxwell-Boltzmann distribution

In the passing we briefly discuss the modified version of Maxwell-Boltzmann velocity distribution in the galactic frame, truncated at the galaxy escape velocity $v_{\rm esc}$. This can be written in the form:

$$f(\mathbf{v}) = \begin{cases} \frac{1}{N}\left[\exp\left(-\frac{|\mathbf{v}|^2}{v_0^2}\right) - \beta \exp\left(-\frac{v_{\rm esc}^2}{v_0^2}\right)\right] & |\mathbf{v}| \leq v_{\rm esc} \\ 0 & |\mathbf{v}| > v_{\rm esc}, \end{cases} \tag{9}$$

where the symbols have their usual meaning. In this work $\beta = 1$ has been chosen with the desire for an exponential cut-off. We use the fiducial values of the SHM to generate the exclusion curves. The exclusion bounds for this distribution of DM are shown by the extra spaced dashed lines in figure 1. Since we have chosen the fiducial values for v_0 and $v_{\rm esc}$, therefore we do not observe any significant changes in the exclusion bound as compared to the standard MB distribution.

4 Beyond the Standard Halo Model

Recent high resolution cosmological N-body simulations like Via Lactea [52], Aquarius [32], GHALO [53], Eris [54], Ling et al [55], etc[3] suggest a tension in the simulated DM distribution within the Galactic halo to what has been predicted from the SHM. Most prominently at the high velocity tail of the DM distribution [55]. Due to the sharp cut off at the escape velocity, the SHM over predicts the number of high energetic DM particles that are available for scattering. A possibility in this regard is to look for a non-SHM distribution of DM motivated by N-body simulations. In what follows we have considered some of these distributions and their implications on the DM-electron scattering rates in direct detection experiments. We study how they modify the exclusion limits in these experiments.

4.1 King Model

For a physical system of finite size, the truncated MB distribution, given in equation (7) may not be a natural solution of collision-less Boltzmann equation. The King distribution [56] is an alternate model which can be formulated self-consistently for a finite size DM halo. In this model instead of the escape velocity, the maximum DM particle velocity $v_{\rm max}$ determines the cut-off criterion ($v_{\rm max} < v_{\rm esc}$). It is predicted on the assumption that if a DM particle moves with $v_{\rm max}$ at any position of the halo then it can reach the halo boundary where by construction the density vanishes [57]. This boundary is often called the truncated radius which represents the physical size of a halo. Such a finite size halo provides a more realistic description of galaxies as compared to the isothermal sphere. These so called lowered isothermal model is also preferred by the recent N-body simulation [58]. The distribution function can be written as

$$f(\mathbf{v}) = \begin{cases} \frac{1}{N}\left[\exp\left(\frac{v_{\rm esc}^2 - |\mathbf{v}|^2}{v_0^2}\right) - 1\right] & |\mathbf{v}| \leq v_{\rm max} \\ 0 & |\mathbf{v}| > v_{\rm max}, \end{cases} \tag{10}$$

where the symbols have their usual meaning. Equating $v_{\rm max}$ with the maximum velocities reported by the N-body simulations provides a reasonable estimate. The best fit values of the parameters for the considered simulations are provided in table 1. The corresponding shift in the exclusion curves are shown in figure 3 for contact interaction ($F_{\rm DM} = 1$) between DM and electron. The variation for the other types of interactions are shown in appendix B.

The special feature observed around the DM mass of 50 MeV on the fiducial SHM curve in figure 3a is originating from the atomic structure of the Xenon atom. This is because around the aforesaid mass the maximum accessible DM energy crosses a threshold to ionize electrons from inner shell. This leads to an increment in the event rate and subsequently the bound becomes tighter. Further, as can be seen from figure 3a, compared to fiducial values this special feature shift towards higher mass for a lower choice of v_0. Note that as v_0 decreases the DM population in the high velocity region decreases substantially. Due to this unavailability of high velocity DM the required DM mass shift towards higher mass to overcome a certain threshold. While for a semiconductor target, recoil electrons need to overcome only one energy barrier i.e. the energy gap between valance band and conduction band. Hence we do not observe such features in figure 3b and 3c. The apparent spike in the lower left panel of figure 3d is a manifestation of the offset between the two kinks of the SHM and the King distribution.

[3] We have provided brief details of the simulations used in this paper in appendix A.

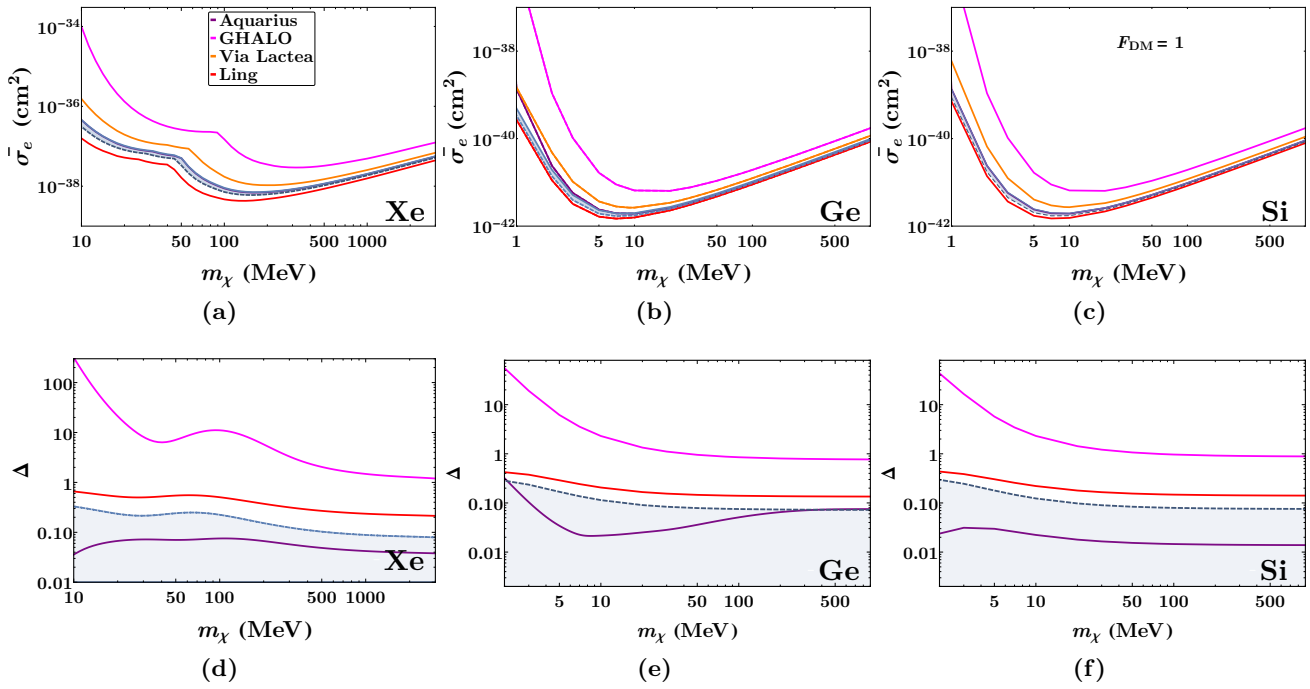

Figure 3: Variations in the exclusion bounds for the King distribution with $F_{\rm DM} = 1$. The variations for Xenon, Germanium and Silicon target materials are shown in the left, middle and right panels respectively. The purple, magenta, orange and red curves corresponds to the Aquarius, GHALO, Via Lactea and Ling simulations respectively with best-fit values from table 1. In the upper panel we show the shifts in the exclusion bounds, while the lower panel show the relative fractional changes (defined in equation (8)) from the GHALO (solid magenta), Ling (solid red) and Aquarius (solid purple) simulations. Note that the light shaded region represents the fractional relative change related to the blue shaded regions in figure 1.

As indicated in table 1, the best fit values of v_0 and $v_{\rm esc}$ for GHALO simulation are smaller than the fiducial values. Due to this in the high velocity region a less number of DM particles are available to interact with the electrons. This leads to weaker bounds in DM electron cross section. This has been shown by the solid magenta curve in figure 3. The best fit v_0 for Ling simulations is substantially larger than the fiducial values. Therefore it sets a stronger bound as shown by the red solid lines in figure 3. The best fit values for Aquarius (solid purple line) and Via Lactea (solid orange line) lie close to fiducial value, implying exclusion limits close to the fiducial exclusion curve. The blue shaded region in figure 3 shows the uncertainties within the SHM, discussed in section 3.

We note that the minimum deviation induced by the N-body motivated King's model is around 1% for Xe atomic detector whereas it can be $\sim 10\%$ and 1% for Ge and Si semiconductor detector respectively. This corresponds to the best fit values of the state-of-the-art N-body simulation Aquarius. In contrast to that the best fit values of simple DM only simulation, GHALO seems to produce a large deviation from SHM.

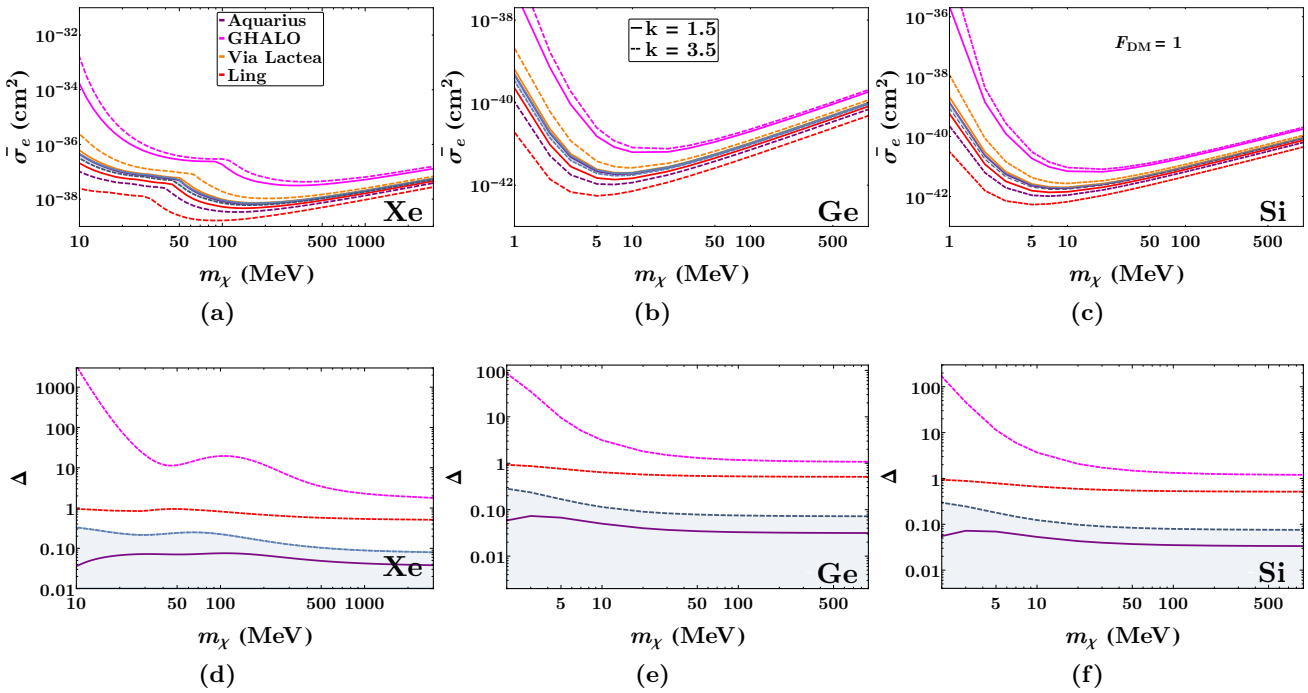

Figure 4: Variations in the exclusion bounds for the Double power law with $F_{\rm DM} = 1$. (a,b,c) The solid and dashed curves correspond to $k = 1.5$ and $k = 3.5$ respectively. In the lower panel we show the relative fractional change for the GHALO (magenta), Ling (dashed red) and Aquarius (solid purple) simulations corresponding to the three set of target materials. The other relevant details are same as of figure 3.

4.2 Double Power Law

The Double Power Law (DPL) distribution is an isotropic distribution of DM which have been obtained empirically [22]. The DPL very well describes the empirical matter distributions such as NFW, Hernquist, etc [22]. The matter distribution of a generic empirical double power law has the form

$$\rho(r) = \frac{\rho_s}{(\frac{r}{r_s})^\alpha (1 + \frac{r}{r_s})^{\gamma-\alpha}}, \tag{11}$$

where r_s is the characteristic radius, ρ_s is the characteristic density, α and γ determines the slope of the density profile at small and large radii respectively. For $(\alpha, \gamma) = (1,\ 3)$ this reduces to the NFW profile [59] while for $(\alpha, \gamma) = (1,\ 4)$ this reproduces Hernquist profile [60]. The DPL velocity distribution is expressed by the form

$$f(\mathbf{v}) = \begin{cases} \frac{1}{N}\left[\exp\left(\frac{v_{\rm esc}^2 - |\mathbf{v}|^2}{k v_0^2}\right) - 1\right]^k & |\mathbf{v}| \le v_{\rm esc} \\ 0 & |\mathbf{v}| > v_{\rm esc}, \end{cases} \tag{12}$$

where the symbols have their usual meaning. N-body simulations which take into account the quasi-static equilibrium nature of the virialised objects [35] and it's formation history attributed from hierarchical merging, smooth accretion and violent relaxations [61] favour such distribution [22]. Unlike

Simulation	$v_{\rm esc}$ (km/s)	DPL		King
		$k = 1.5$	$k = 3.5$	v_o (km/s)
		v_o (km/s)	v_o (km/s)	
GHALO [53]	433	150.6	146.5	152
Aquarius [32]	565	230.7	344.6	223.7
Via Lactea [52]	550	223.7	212.4	196.5
Ling et al [55]	520	275	486	254.7

Table 1: Best fit values used to derive the exclusion limit for DPL and King model. The best fit values for both model are adapted from [22].

the SHM, the velocity distribution in DPL smoothly goes to zero at the escape velocity. Thus it differs in the high velocity tail region from the SHM and predicts lower number of DM particles near the tail of the velocity distribution.

Numerical simulations suggest that γ of the density distributions in equation (11) ranges between 3 to 5 [62], where γ can be related to k in equation (12) though the Eddingtion formalism [63] by the relation $k = \gamma - \frac{3}{2}$ [64]. Hence k ranges between 1.5 to 3.5. For $k \to 0$ it reduces to the SHM and for $k = 1$ it tends to the King distribution. The best fit parameters from state-of-the-art Cosmological N-body simulations, that have been used in this work are given in table 1.

Note that the DPL distribution can be viewed as a generalization of the King model, described in section 4.1. Therefore the impact on electron recoil events rate here would be similar to what has been discussed in section 4.1. The difference here is in the power index k which vary in the range 1.5 to 3.5, as compared to $k = 1$ for the King model. Any change in the numerical value of k would proportionally change the event rate and subsequently the direct detection limits. This can also be understood by comparing the relative fractional change in cross section depicted in lower panel of the figures 3 and 4. Like figure 3, in figure 4 the purple, magenta, orange and red coloured lines corresponds to the Aquarius, GHALO, Via Lactea and Ling simulations respectively.

For DPL we find that for the more sophisticated N-body simulation a deviation of $\sim 5\%$ for Xe and $\sim 10\%$ both the Ge and Si semiconductor detector are obtained. This deviation is fairly flat in the DM mass range of interest.

4.3 Tsallis

The Tsallis distribution is explicitly derived through a factorization approximation of the Tsallis statistics [25] which is a generalisation of Boltzmann-Gibbs entropy. The distribution is widely used in high energy collisions [65], Bose-Einstein condensation [66], black-body radiation, neutron star [67], early universe cosmology [68] and superconductivity [69]. The velocity distribution function goes by the form

$$f(\mathbf{v}) = \begin{cases} \frac{1}{N}\left[1 - (1-q)\frac{|\mathbf{v}|^2}{v_0^2}\right]^{\frac{1}{1-q}} & |\mathbf{v}| \leq v_{\rm esc} \\ 0 & |\mathbf{v}| > v_{\rm esc}, \end{cases} \tag{13}$$

where the symbols have their usual meaning. For this distribution with $q < 1$ the escape velocity is determined by the relation $v_{\rm esc}^2 = v_0^2/(1-q)$. This inherent cut off criterion makes this distribution

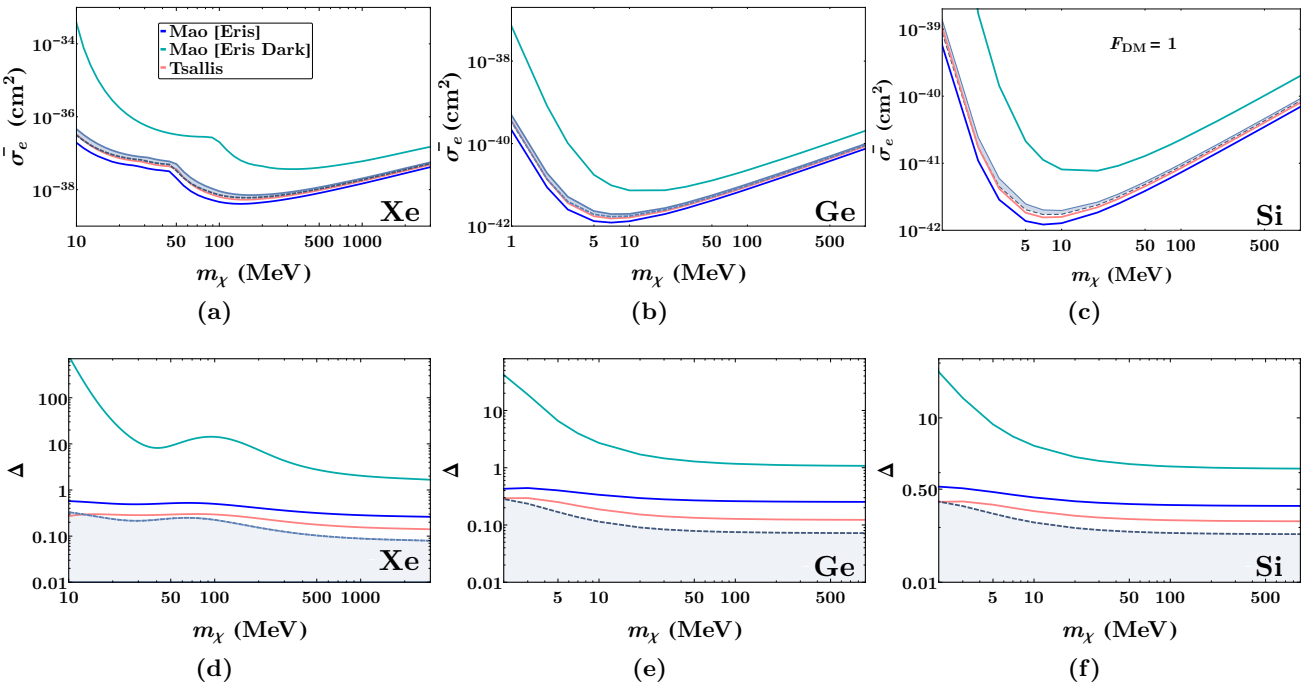

Figure 5: Variations in the exclusion bounds for Tsallis and Mao et. al. with $F_{\rm DM} = 1$. In the upper panel, the blue, cyan and pink curves corresponds to the exclusion bounds for Mao et. al. (with Eris), Mao et. al. (with Eris dark), Tsallis respectively. Best fit values for Mao distribution are given in table 2, while for the Tsallis the best parameters are provided in section 4.3. In the lower panel the relative fractional change (Δ) for Mao with Eris simulation (blue) and Mao with Eris dark simulation (cyan) and Tsallis distributions (pink) have been shown. The other relevant details are same as of figure 3.

appealing as compared to the SHM. While for $q > 1$ escape velocity still remains a somewhat arbitrary parameter. In $q \to 1$ limit the Tsallis distribution reduces to the Gaussian form of the SHM. Further from equation (13) it is evident that this distribution predicts a continuous and smooth fall near the tail, favoured by cosmological simulations [31,32,55]. In particular, it has been argued in reference [55] the Tsallis distribution seems to fit better with Milky Way like N-Body simulations including Baryonic physics. The best fit parameters from the Ling et. al. simulations are $v_{\rm esc} = 560.8\,{\rm km/s}, v_0 = 267.2\,{\rm km/s}$, $q = 0.773$ [55].

The bound on $\overline{\sigma}_e$ considering Tsallis as the distribution for DM is presented by the pink curve in figure 5. This bound is obtained by using the best fit values mentioned above. We do not observe any significant variation from SHM in this case.

4.4 Mao et. al.

Mao et. al. [70] postulates an empirical model for the velocity distribution of DM having a wider peak and a steeper tail in comparison to the MB distribution. The Mao distribution function is given by

$$f(\mathbf{v}) = \begin{cases} \frac{1}{N}\left[\left(v_{\rm esc}^2 - |\mathbf{v}|^2\right)^p e^{-\frac{v}{v_0}}\right] & |\mathbf{v}| \leq v_{\rm esc} \\ 0 & |\mathbf{v}| > v_{\rm esc}, \end{cases} \tag{14}$$

where the symbols have their usual meaning. It is favoured by the simulations that have taken into account the sequence of mergers, violent-relaxation and accretion in the simulated halos [71]. Unlike other variants of the SHM, this empirical model is not based on a Gaussian but rather on an exponential distribution function having a power law cut-off in the binding energy or the equivalent escape velocity.

From the MW-like Eris and ErisDark halo simulations, the best fit parameters that have been adopted from [72] and have been used in this work are given in table 2.

Simulation	$v_{\rm esc}$ (km/s)	v_o (km/s)	p
Eris	480	330	2.7
ErisDark	440	100	1.5

Table 2: Best fit parameters for Mao et. al [72].

Assuming Mao as the velocity distribution for DM, in figure 5 we have presented the shift in the exclusion limit. The blue curve corresponds to the best fit Eris simulation while the dark green curve corresponds to the best fit Eris dark simulation. It is clear that compared to the fiducial SHM, the dark green and blue curves set weaker and stronger bounds on DM-electron scattering respectively. This is mainly due to the large difference between the best fit values of v_0 and the fiducial values of the SHM. Note that the Eris simulation takes into account the baryonic contribution and the best fit exclusion bound for this does not have much deviation from the fiducial curve. For the Eris dark simulation the shift in the cross section is greater than the SHM.

For the best fit DM only Eris Dark simulation we observe a significant deviation from the SHM. Further the best fit Eris simulation which takes into account baryonic contribution shows a maximum 70% change for Xe and 40% (50%) change for Ge (Si) detector. This signify the correlation between the bounds and the nature of the underlying fitted N-body simulation details.

4.5 Implications of N-body Simulations

In this sub-section we explored the effects of the various N-body simulations on the derived bounds. Considering distributions like King and DPL in sections 4.1 and 4.2 respectively, we observe the fit to GHALO simulation provide the maximum deviation of $\Delta \sim \mathcal{O}(10)$ from SHM as apparent from figures 3 and 4. Note that the GHALO simulation has only considered DM particles, whereas the Aquarius simulation has considered both the DM and baryonic content along with the halo formation history in their simulation. Interestingly, the best fit bound from Aquarius lie in close proximity to the fiducial SHM curve with a deviation of $\Delta \sim \mathcal{O}(10^{-1})$. As stated in appendix A, the Aquarius has a force

resolution of 20.5 pc whereas Ling et al. which has also considered the effects of Baryons and structure formation have been simulated with a force resolution of 200 pc. Comparing the bounds between the Ling and Aquarius simulations, it can be inferred that best fit values of the high resolution simulations tend to mimic the fiducial bounds of the SHM.

The effect of baryons becomes evident if we observe the exclusion curves of the Mao distribution in figure 5 with best-fit parameters from Eris and Eris dark simulations. Although both of these simulations have the same force resolution of 150 pc [54], bound from the DM only Eris dark simulation shows a maximum deviation of the $\Delta \sim \mathcal{O}(10)$ from the fiducial SHM bound. Whereas the bounds from Eris simulation which take into the baryons, remain closer to the fiducial SHM. This tend to imply that the results of this section should be interpreted keeping in mind the general accuracy and resolution of the underlying N-body simulations.

5 Conclusion

The non-observation of DM in the typical nuclear recoil direct detection experiments and the inability of GeV scale cold DM to address certain small scale structure formation issues has increased the interest in sub-GeV scale DM. An elegant avenue to probe such light DM is to consider the scattering of DM with electron in the direct detection experiments. Bounds on DM electron cross section are typically presented assuming the SHM for DM distribution in our galaxy, with a fiducial choice for $v_0 = 220$ km/s and $v_{\rm esc} = 544$ km/s. However, recent progress in the measurement of these parameters shows a deviation from these values. In this paper we have systematically investigated the effects of uncertainties associated with the determination of these astrophysical quantities on the exclusion limits of DM electron cross section. We consider the uncertainties within the SHM and empirical models of DM distribution beyond the SHM that have been motivated by recent high resolution N-body simulation of the Milky way galaxy.

We find that the exclusion bounds are expectedly sensitive to the population of DM particles in the high velocity tails of the distributions. Within the SHM the velocity distribution is assumed to be MB like. The tail shape is controlled by the Sun's circular velocity (v_0) and to a lesser extent by the escape velocity ($v_{\rm esc}$). We find that within SHM for contact interaction between DM and electron, these uncertainties imply upto $\sim 35\%$ change in the event rates in all the three target materials that have been considered. Further, inclusion of uncertainties in the local DM density leads to additional change in the exclusion bounds.

Going beyond the SHM, N-body simulation motivated we have considered the King's model, Double Power Law, Mao, and Tsallis. Relative to SHM all these non-SHM model falls smoothly near the high velocity tail therefore predicts a less number particles in this region. This subsequently causes a reduction in the event rate. Further for these models depending on fitted parameters we find that in the most region of the parameter space the fractional changes in the cross section could vary substantially. Interestingly the amount of deviations observed from N-body simulations fits can be traced to their treatment of baryonic content and force resolution in their simulation. High resolution simulations with careful treatment of baryonic content and merger histories are observed to be in closer agreement with SHM predictions. The shift from the fiducial choice within SHM to these models leads to conservative deviations in the range of $1\% - 15\%$ for high resolution sophisticated simulations.

Note added: While this paper was under preparation a related work [73] appeared in the arXiv. Their treatment of halo uncertainties for semiconductor targets with Tsallis and Mao distribution is complementary with our discussion in section 4.

Acknowledgements : TNM acknowledges the Department of Science and Technology, Government of India, under the Grant Agreement No. ECR/2018/002192 (Early Career Research Award) for financial assistance. SS acknowledges the University Grants Commission (UGC) of the Government of India for providing financial assistance through Senior Research Fellowship (SRF) with reference ID: 522157.

A A Brief detail of N-body Simulations

In this appendix we briefly summarize the N-body simulations used in this paper.

A.1 Aquarius

The initial cosmological parameters for the Aquarius simulation are set from the WMAP 5-year data analysis. The cosmological simulations used 900^3 particles to follow a DM distribution in a $100/h$ Mpc periodic box. Halos were selected having masses $\approx 10^{10} M_\odot$ and which had no close and massive neighbours at $z = 0$. These include a sample of 6 ultra-highly resolved Milky-way sized halos, allowing to estimate the halo-to-halo scattering substructure statistics. The Aq-A-1 is the highest resolution calculation, with a particle mass of $1.712103\, M_\odot$ and a virial mass of $1.839 \times 10^{10} M_\odot$. It has more than a billion particles within the virial radius. It is defined as the radius containing a mean density of 200 times the critical density value. The Plummer equivalent softening length of this run is 20.5 pc [32]. The Aquarius project used the parallel simulation code GADGET [74].

A.2 Illustris

The IllustrisTNG [51,75] project is a publicly available suite of state-of-the-art magneto-hydrodynamic cosmological simulations. The cosmological parameters used in these simulations were chosen from the analysis of the Plank Collaboration. It uses the moving mesh hydrodynamics code AREPO. It has been argued that the Milky Way like galaxies of the IllustrisTNG reproduced the observed Milky-way rotation curve adequately. This suggests that the matter distribution in the simulated MW galaxies tend to be realistic. Halos are selected from a $75/h = 110.7$ Mpc box. The baryon and dark matter mass resolutions are $M_{\rm baryon} = 1.4 \times 10^6 M_\odot$ and $M_{\rm DM} = 7.5 \times 10^6 M_\odot$ respectively. The galaxies are chosen in the mass range $5 \times 10^{11} M_\odot \leq M_{\rm virial}/M_\odot \leq 2 \times 10^{12} M_\odot$, stellar mass range $2.5 \times 10^{10} M_\odot \leq M_*/M_\odot \leq 5 \times 10^{10} M_\odot$ and the gaseous mass to stellar mass fraction in the range $0.03 \leq M_{\rm gas}/M_* \leq 1$. The selected galaxies do not have any significant merger effects after a redshift of $z = 0.68$, giving 164 galaxy halos for the study.

A.3 GHALO

The GHALO project involves a series of Milky Way like DM halo simulations at different resolutions. The largest of them uses 3.1×10^9 particles having a mass resolution of $1000 M_\odot$. It measures the density profile to a distance of 120 pc, which is (0.05% of its virial radius ($R_{\rm vir}$)). The halos of mass $10^{12} M_\odot$ and radius $R_{\rm vir} = 240$ kpc were selected from a cube of cosmological simulation of length 40 Mpc. The final effective resolution of $\rm GHALO_2$ has been simulated with 13176^3 particles, having $R_{\rm vir} = 347$ kpc. Which has been used for this work. GHALO project uses the gravity code PKDGRAV2, a parallel computing code alongside a fast multi-pole method [53].

A.4 Ling

The Ling et. al. describes Milky Way sized halos including gas, stars and DM in high-resolution cosmological N-body simulations at the present redshift ($z = 0$). Its resolution is sufficient to witness the formation of a rotating disk and a bulge at the center of the halo. The velocity distributions obtained from fits with the simulation show strong deviations from a pure Gaussian and Maxwellian distributions having a sharper drop at the high velocity tail. The simulations were performed using the cosmological Adaptive Mesh Refinement code RAMSES, using the "zoom-in" simulation technique and a Cartesian grid of 1024^3 elements covering a 20 Mpc/h periodic box. The spatial resolution has been set to be 200 pc and $R_{\rm vir} = 264$ kpc. It contains $N_{\rm DM} = 842,768$ corresponding to a halo mass of $6.3 \times 10^{11} M_\odot$. Halos with mass accretion history typically of a late-type galaxy, with no major merger and a steady accretion rate in the last 8 Gyr have been selected for obtaining the fits used in this simulation. The central galaxy has a bulge mass of $4 \times 10^{10} M_\odot$ with a similar disc mass [55].

A.5 Via Lactea

The Via Lactea simulations use the parallel tree code PKDGRAV2 and 1.1×10^9 particles of mass $4,100 M_\odot$. The simulation follows the growth of a Milky Way-size halo in a ΛCDM Universe from a redshift of 104.3. It uses the cosmological parameters from WMAP analysis to set the initial conditions of the simulation. It has resolved over $40,000$ sub-halos within a distance of 402 kpc from the center of the MW sized halos. These simulations along-with its estimates assume that the gravitational effects of baryons on the DM to be small [52].

A.6 Eris

The Eris project involves a twin set of Nbody and hydro-dynamic simulations. They have selected disk galaxies that match many of the observed properties of our Milky Way in both the Eris and its DM-only twin, the ErisDark. The collision less runs for both start from identical initial conditions, allowing to isolate the effects of dissipative baryonic physics on galaxy formation. The total mass of the resulting simulated galaxy chosen is $8 \times 10^{11} M_\odot$. Both Eris and ErisDark are cosmological zoom-in simulations of a Milky-Way-like galaxy drawn from an N-body realization of 4×10^{10} DM particles in a 90/h Mpc side periodic box. The initial conditions have been generated with the code GRAFIC, assuming first-order Zeld'ovich approximation for the displacements and velocities of the

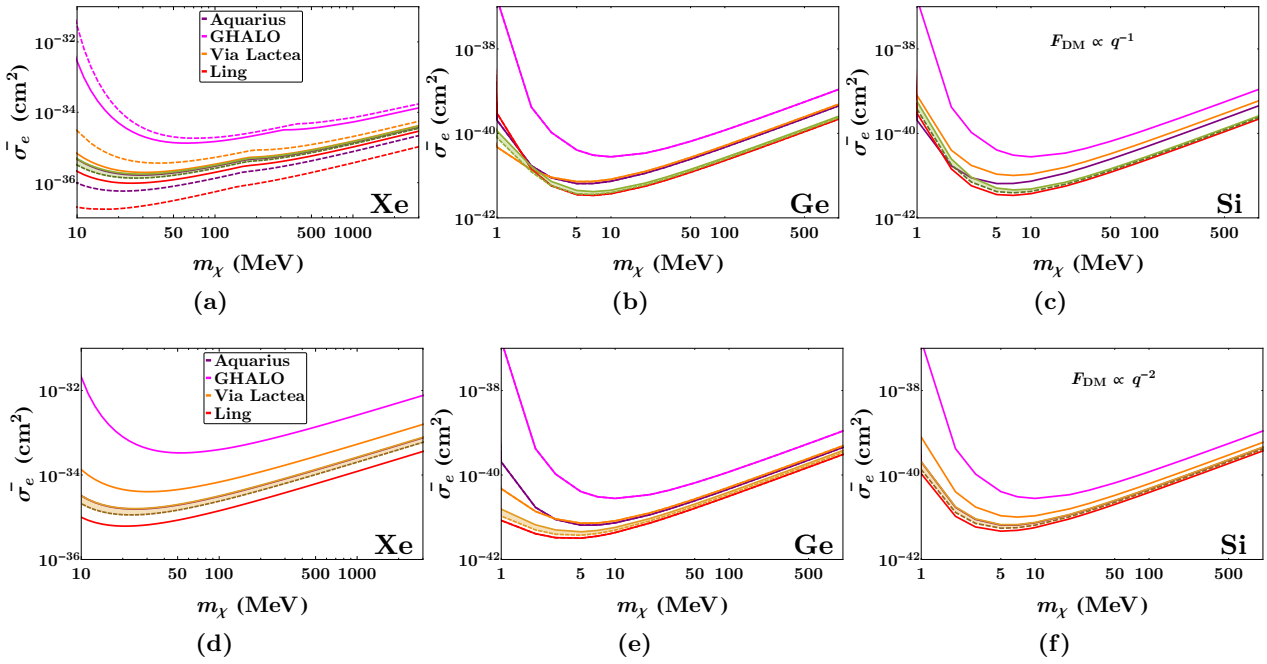

Figure 6: Variations in the exclusion bounds for King distribution: Upper panel shows the variations for $F_{\rm DM} \propto q^{-1}$ and the lower panel shows the variations for $F_{\rm DM} \propto q^{-2}$. The other relevant details are same as of figure 3.

particles at $z = 90$. The simulations use particles of mass $1.2 \times 10^{10} M_\odot$ in a sub region of about 1 Mpc side. Eris and ErisDark are simulated with the SPH/Nbody code GASOLINE. In the Eris SPH simulation, presented in [54], aiming at a high-resolution the particles are further split into 13×10^6 DM particles and an equal number of gas particles. The mass resolution of DM and gas particle are $m_{\rm DM} = 9.8 \times 10^4 M_\odot$ and $m_{\rm SPH} = 2 \times 10^4 M_\odot$ respectively. Each star particle is stochastically created with an initial mass of $m_* = 6.1 \times 10^3 M_\odot$. The stellar mass contained in the thin disk is $2 \times 10^{10} M_\odot$ which is 50% of the overall stellar content at $z = 0$.

B Momentum dependent DM-electron interactions

In this appendix we have presented the shift in the exclusion limit for other two choices of interactions between DM and electron namely $F_{\rm DM} \propto q^{-1}$ and $F_{\rm DM} \propto q^{-2}$. In figures 6, 7 we have provided variation for King and DPL model respectively. The bound from the rest of the non-SHM distribution considered here in shown in figure 8. For each of the figures the upper panel corresponds to $F_{\rm DM} \propto q^{-1}$ and lower panel corresponds to $F_{\rm DM} \propto q^{-2}$. For Xe targets the momentum suppression in the momentum dependence interaction shifts the special feature (discussed in section 4.1) towards higher DM mass. While for $F_{\rm DM} \propto q^{-1}$ this appears around DM mass of 200 MeV however for $F_{\rm DM} \propto q^{-2}$ this crosses the boundary of figure, as has been depicted in the left panels of figures 6, 7, and 8.

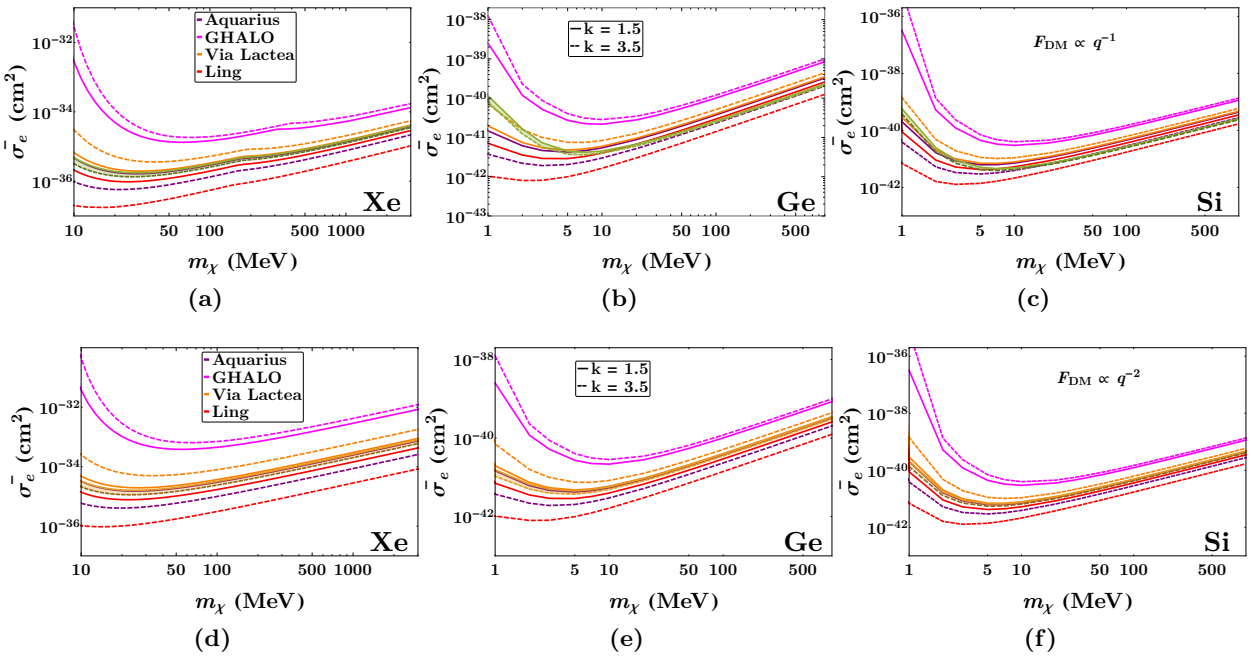

Figure 7: Variations in the exclusion bounds for the DPL distribution : Upper panel shows the variations for $F_{\rm DM} \propto q^{-1}$ and the lower panel shows the variations for $F_{\rm DM} \propto q^{-2}$. The other relevant details are same as of figure 4.

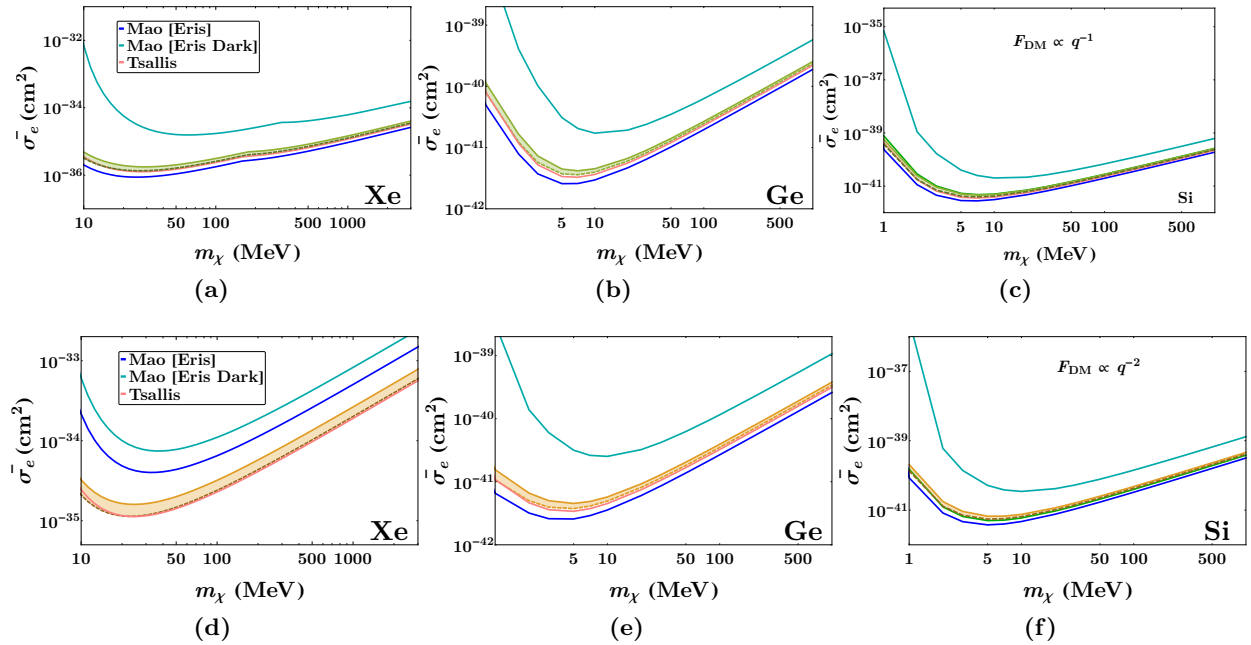

Figure 8: Variations in the exclusion bounds for the Mao, Tsallis & MMB distributions: Upper panel shows the variations for $F_{\rm DM} \propto q^{-1}$ and the lower panel shows the variations for $F_{\rm DM} \propto q^{-2}$. The other relevant details are same as of figure 5.

References

[1] M. W. Goodman and E. Witten, *Detectability of Certain Dark Matter Candidates*, *Phys. Rev. D* **31** (1985) 3059.

[2] A. Drukier, K. Freese and D. Spergel, *Detecting Cold Dark Matter Candidates*, *Phys. Rev. D* **33** (1986) 3495–3508.

[3] S. Profumo, *An Introduction to Particle Dark Matter*. World Scientific, 2017, 10.1142/q0001.

[4] J. Silk et al., *Particle Dark Matter: Observations, Models and Searches*. Cambridge Univ. Press, Cambridge, 2010, 10.1017/CBO9780511770739.

[5] G. Arcadi, M. Dutra, P. Ghosh, M. Lindner, Y. Mambrini, M. Pierre et al., *The waning of the WIMP? A review of models, searches, and constraints*, *Eur. Phys. J. C* **78** (2018) 203, [1703.07364].

[6] J. Lewin and P. Smith, *Review of mathematics, numerical factors, and corrections for dark matter experiments based on elastic nuclear recoil*, *Astropart. Phys.* **6** (1996) 87–112.

[7] XENON collaboration, E. Aprile et al., *Dark Matter Search Results from a One Ton-Year Exposure of XENON1T*, *Phys. Rev. Lett.* **121** (2018) 111302, [1805.12562].

[8] LUX collaboration, D. S. Akerib et al., *Results on the Spin-Dependent Scattering of Weakly Interacting Massive Particles on Nucleons from the Run 3 Data of the LUX Experiment*, *Phys. Rev. Lett.* **116** (2016) 161302, [1602.03489].

[9] PandaX-II collaboration, X. Cui et al., *Dark Matter Results From 54-Ton-Day Exposure of PandaX-II Experiment*, *Phys. Rev. Lett.* **119** (2017) 181302, [1708.06917].

[10] R. Essig, J. Mardon and T. Volansky, *Direct Detection of Sub-GeV Dark Matter*, *Phys. Rev. D* **85** (2012) 076007, [1108.5383].

[11] R. Essig, A. Manalaysay, J. Mardon, P. Sorensen and T. Volansky, *First Direct Detection Limits on sub-GeV Dark Matter from XENON10*, *Phys. Rev. Lett.* **109** (2012) 021301, [1206.2644].

[12] R. Essig, M. Fernandez-Serra, J. Mardon, A. Soto, T. Volansky and T.-T. Yu, *Direct Detection of sub-GeV Dark Matter with Semiconductor Targets*, *JHEP* **05** (2016) 046, [1509.01598].

[13] S. K. Lee, M. Lisanti, S. Mishra-Sharma and B. R. Safdi, *Modulation Effects in Dark Matter-Electron Scattering Experiments*, *Phys. Rev. D* **92** (2015) 083517, [1508.07361].

[14] R. Essig, T. Volansky and T.-T. Yu, *New Constraints and Prospects for sub-GeV Dark Matter Scattering off Electrons in Xenon*, *Phys. Rev. D* **96** (2017) 043017, [1703.00910].

[15] http://ddldm.physics.sunysb.edu/ddlDM/.

[16] M. C. Smith et al., *The RAVE Survey: Constraining the Local Galactic Escape Speed*, *Mon. Not. Roy. Astron. Soc.* **379** (2007) 755–772, [astro-ph/0611671].

[17] A. M. Green, *Astrophysical uncertainties on the local dark matter distribution and direct detection experiments*, *J. Phys. G* **44** (2017) 084001, [1703.10102].

[18] C. Kelso, C. Savage, M. Valluri, K. Freese, G. S. Stinson and J. Bailin, *The impact of baryons on the direct detection of dark matter*, *JCAP* **08** (2016) 071, [1601.04725].

[19] J. D. Sloane, M. R. Buckley, A. M. Brooks and F. Governato, *Assessing Astrophysical Uncertainties in Direct Detection with Galaxy Simulations*, *Astrophys. J.* **831** (2016) 93, [1601.05402].

[20] B. J. Kavanagh, *Parametrizing the local dark matter speed distribution: a detailed analysis*, *Phys. Rev. D* **89** (2014) 085026, [1312.1852].

[21] S. K. Lee, *Harmonics in the Dark-Matter Sky: Directional Detection in the Fourier-Bessel Basis*, *JCAP* **03** (2014) 047, [1401.6179].

[22] M. Lisanti, L. E. Strigari, J. G. Wacker and R. H. Wechsler, *The Dark Matter at the End of the Galaxy*, *Phys. Rev. D* **83** (2011) 023519, [1010.4300].

[23] Y.-Y. Mao, L. E. Strigari and R. H. Wechsler, *Connecting Direct Dark Matter Detection Experiments to Cosmologically Motivated Halo Models*, *Phys. Rev. D* **89** (2014) 063513, [1304.6401].

[24] J. Binney and S. Tremaine, *Galactic Dynamics: Second Edition*. 2008.

[25] C. Tsallis, *Possible Generalization of Boltzmann-Gibbs Statistics*, *J. Statist. Phys.* **52** (1988) 479–487.

[26] N. W. Evans, C. A. O'Hare and C. McCabe, *Refinement of the standard halo model for dark matter searches in light of the Gaia Sausage*, *Phys. Rev. D* **99** (2019) 023012, [1810.11468].

[27] E. Izaguirre, G. Krnjaic, P. Schuster and N. Toro, *Analyzing the Discovery Potential for Light Dark Matter*, *Phys. Rev. Lett.* **115** (2015) 251301, [1505.00011].

[28] B. Holdom, *Two U(1)'s and Epsilon Charge Shifts*, *Phys. Lett. B* **166** (1986) 196–198.

[29] K. Sigurdson, M. Doran, A. Kurylov, R. R. Caldwell and M. Kamionkowski, *Dark-matter electric and magnetic dipole moments*, *Phys. Rev. D* **70** (2004) 083501, [astro-ph/0406355].

[30] R. Schönrich, J. Binney and W. Dehnen, *Local kinematics and the local standard of rest*, *Monthly Notices of the Royal Astronomical Society* **403** (Apr, 2010) 1829–1833.

[31] M. Kuhlen, N. Weiner, J. Diemand, P. Madau, B. Moore, D. Potter et al., *Dark Matter Direct Detection with Non-Maxwellian Velocity Structure*, *JCAP* **02** (2010) 030, [0912.2358].

[32] M. Vogelsberger, A. Helmi, V. Springel, S. D. White, J. Wang, C. S. Frenk et al., *Phase-space structure in the local dark matter distribution and its signature in direct detection experiments*, *Mon. Not. Roy. Astron. Soc.* **395** (2009) 797–811, [0812.0362].

[33] XENON10 collaboration, J. Angle et al., *A search for light dark matter in XENON10 data*, *Phys. Rev. Lett.* **107** (2011) 051301, [1104.3088].

[34] P. J. T. Leonard and S. Tremaine, *The Local Galactic Escape Speed*, *apj* **353** (Apr., 1990) 486.

[35] D. Lynden-Bell, *Statistical mechanics of violent relaxation in stellar systems*, *Mon. Not. Roy. Astron. Soc.* **136** (1967) 101–121.

[36] A. Hryczuk, E. Karukes, L. Roszkowski and M. Talia, *Impact of uncertainties in the halo velocity profile on direct detection of sub-GeV dark matter*, 2001.09156.

[37] E. Andersson, A. Bökmark, R. Catena, T. Emken, H. K. Moberg and E. Åstrand, *Projected sensitivity to sub-GeV dark matter of next-generation semiconductor detectors*, *JCAP* **05** (2020) 036, [2001.08910].

[38] Particle Data Group collaboration, P. Zyla et al., *Review of Particle Physics*, *PTEP* **2020** (2020) 083C01.

[39] M. Pato, F. Iocco and G. Bertone, *Dynamical constraints on the dark matter distribution in the Milky Way*, *JCAP* **12** (2015) 001, [1504.06324].

[40] P. Salucci, F. Nesti, G. Gentile and C. Martins, *The dark matter density at the Sun's location*, *Astron. Astrophys.* **523** (2010) A83, [1003.3101].

[41] R. Catena and P. Ullio, *A novel determination of the local dark matter density*, *JCAP* **08** (2010) 004, [0907.0018].

[42] SuperCDMS collaboration, R. Agnese et al., *Search for Low-Mass Weakly Interacting Massive Particles with SuperCDMS*, *Phys. Rev. Lett.* **112** (2014) 241302, [1402.7137].

[43] LUX collaboration, D. Akerib et al., *Results from a search for dark matter in the complete LUX exposure*, *Phys. Rev. Lett.* **118** (2017) 021303, [1608.07648].

[44] S. E. Koposov, H.-W. Rix and D. W. Hogg, *Constraining the Milky Way potential with a 6-D phase-space map of the GD-1 stellar stream*, *Astrophys. J.* **712** (2010) 260–273, [0907.1085].

[45] P. J. McMillan and J. J. Binney, *The uncertainty in Galactic parameters*, *Mon. Not. Roy. Astron. Soc.* **402** (2010) 934, [0907.4685].

[46] M. J. Reid and A. Brunthaler, *The Proper motion of Sgr A*. 2. The Mass of Sgr A**, *Astrophys. J.* **616** (2004) 872–884, [astro-ph/0408107].

[47] J. Bland-Hawthorn and O. Gerhard, *The galaxy in context: Structural, kinematic, and integrated properties*, *Annual Review of Astronomy and Astrophysics* **54** (Sep, 2016) 529–596.

[48] GRAVITY collaboration, R. Abuter et al., *Detection of the gravitational redshift in the orbit of the star S2 near the Galactic centre massive black hole*, *Astron. Astrophys.* **615** (2018) L15, [1807.09409].

[49] G. Monari, B. Famaey, I. Carrillo, T. Piffl, M. Steinmetz, R. F. G. Wyse et al., *The escape speed curve of the galaxy obtained from gaia dr2 implies a heavy milky way*, *Astronomy and Astrophysics* **616** (Aug, 2018) L9.

[50] A. J. Deason, A. Fattahi, V. Belokurov, N. W. Evans, R. J. J. Grand, F. Marinacci et al., *The local high-velocity tail and the galactic escape speed*, *Monthly Notices of the Royal Astronomical Society* **485** (Mar, 2019) 3514–3526.

[51] V. Springel et al., *First results from the IllustrisTNG simulations: matter and galaxy clustering*, *Mon. Not. Roy. Astron. Soc.* **475** (2018) 676–698, [1707.03397].

[52] J. Diemand, M. Kuhlen, P. Madau, M. Zemp, B. Moore, D. Potter et al., *Clumps and streams in the local dark matter distribution*, *Nature* **454** (2008) 735–738, [0805.1244].

[53] J. Stadel, D. Potter, B. Moore, J. Diemand, P. Madau, M. Zemp et al., *Quantifying the heart of darkness with GHALO - a multi-billion particle simulation of our galactic halo*, *Mon. Not. Roy. Astron. Soc.* **398** (2009) L21–L25, [0808.2981].

[54] J. Guedes, S. Callegari, P. Madau and L. Mayer, *Forming Realistic Late-Type Spirals in a LCDM Universe: The Eris Simulation*, *Astrophys. J.* **742** (2011) 76, [1103.6030].

[55] F. Ling, E. Nezri, E. Athanassoula and R. Teyssier, *Dark Matter Direct Detection Signals inferred from a Cosmological N-body Simulation with Baryons*, *JCAP* **02** (2010) 012, [0909.2028].

[56] I. R. King, *The Structure of star clusters. 3. Some simple dynamical models*, *Astron. J.* **71** (1966) 64.

[57] S. Chaudhury, P. Bhattacharjee and R. Cowsik, *Direct detection of WIMPs : Implications of a self-consistent truncated isothermal model of the Milky Way's dark matter halo*, *JCAP* **09** (2010) 020, [1006.5588].

[58] F.-S. Ling, E. Nezri, E. Athanassoula and R. Teyssier, *Dark matter direct detection signals inferred from a cosmological n-body simulation with baryons*, *Journal of Cosmology and Astroparticle Physics* **2010** (Feb, 2010) 012–012.

[59] J. F. Navarro, C. S. Frenk and S. D. White, *A Universal density profile from hierarchical clustering*, *Astrophys. J.* **490** (1997) 493–508, [astro-ph/9611107].

[60] L. Hernquist, *An Analytical Model for Spherical Galaxies and Bulges*, *Astrophys. J.* **356** (1990) 359.

[61] J. Wang and S. D. White, *Are mergers responsible for universal halo properties?*, *Mon. Not. Roy. Astron. Soc.* **396** (2009) 709, [0809.1322].

[62] M. T. Busha, A. E. Evrard, F. C. Adams and R. H. Wechsler, *The Ultimate halo mass in a Lambda-CDM Universe*, *Mon. Not. Roy. Astron. Soc.* **363** (2005) L11–L15, [astro-ph/0412161].

[63] A. S. Eddington, *The distribution of stars in globular clusters*, *mnras* **76** (May, 1916) 572–585.

[64] C. S. Kochanek, *The Mass of the Milky Way galaxy*, *Astrophys. J.* **457** (1996) 228, [astro-ph/9505068].

[65] J. Cleymans and M. Azmi, *Large Transverse Momenta and Tsallis Thermodynamics*, *J. Phys. Conf. Ser.* **668** (2016) 012050, [1508.03143].

[66] H. Miller, F. Khanna, R. Teshima, A. Plastino and A. Plastino, *Generalized thermostatistics and bose–einstein condensation*, *Physics Letters A* **359** (2006) 357 – 358.

[67] D. P. Menezes, A. Deppman, E. Megıas and L. B. Castro, *Non-extensive thermodynamics and neutron star properties*, *The European Physical Journal A* **51** (Dec, 2015) .

[68] R. Szczesniak, E. A. Drzazga, I. A. Domagalska, A. P. Durajski and M. Kostrzewa, *Non-parametric application of tsallis statistics to systems consisting of m hydrogen molecules*, 2018.

[69] A. Parvan and T. Bhattacharyya, *Remarks on the phenomenological Tsallis distributions and their link with the Tsallis statistics*, 1904.02947.

[70] Y.-Y. Mao, L. E. Strigari, R. H. Wechsler, H.-Y. Wu and O. Hahn, *Halo-to-Halo Similarity and Scatter in the Velocity Distribution of Dark Matter*, *Astrophys. J.* **764** (2013) 35, [1210.2721].

[71] S. H. Hansen, B. Moore, M. Zemp and J. Stadel, *A Universal velocity distribution of relaxed collisionless structures*, *JCAP* **01** (2006) 014, [astro-ph/0505420].

[72] M. Kuhlen, A. Pillepich, J. Guedes and P. Madau, *The Distribution of Dark Matter in the Milky Way's Disk*, *Astrophys. J.* **784** (2014) 161, [1308.1703].

[73] A. Radick, A.-M. Taki and T.-T. Yu, *Dependence of Dark Matter - Electron Scattering on the Galactic Dark Matter Velocity Distribution*, 2011.02493.

[74] V. Springel, N. Yoshida and S. D. White, *GADGET: A Code for collisionless and gasdynamical cosmological simulations*, *New Astron.* **6** (2001) 79, [astro-ph/0003162].

[75] A. Pillepich et al., *Simulating Galaxy Formation with the IllustrisTNG Model*, *Mon. Not. Roy. Astron. Soc.* **473** (2018) 4077–4106, [1703.02970].